Available online at www.sciencedirect.com
SCIENCE DIRECT®
ELSEVIER
Computers & Fluids 33 (2004) 463–483
computers & fluids
www.elsevier.com/locate/compfluid

An explicit projection method for solving incompressible flows driven by a pressure difference

R. Fernandez-Feria *, E. Sanmiguel-Rojas

Universidad de Málaga, E.T.S. Ingenieros Industriales, 29013 Málaga, Spain

Received 11 April 2002; received in revised form 18 November 2002; accepted 7 April 2003

Abstract

A finite-difference method for solving the incompressible time-dependent three-dimensional Navier–Stokes equations in open flows where Dirichlet boundary condition (BC) for the pressure are given on part of the boundary is presented. The equations in primitive variables $(\mathbf{v}, p)$ are solved using a projection method on a non-staggered grid with second-order accuracy in space and time. On the inflow and outflow boundaries the pressure is obtained from its given value at the contour of these surfaces using a two-dimensional form of the pressure Poisson equation, which enforces the incompressibility constraint $\nabla \cdot \mathbf{v} = 0$. The obtained pressure in these surfaces is used as Dirichlet BCs for the three-dimensional Poisson equation inside the domain. The solenoidal requirement imposes some restrictions on the choice of the open surfaces. However, these restrictions are usually met in most flows of interest driven by a pressure (or a body force) difference, to which the present numerical method is mainly intended. To check the accuracy of the method, it is applied to several examples including the flow over a backward-facing step, and the three-dimensional pressure driven flow in a circular pipe.

Keywords: Pressure boundary conditions; Projection method; Pressure driven flows

1. Introduction

Many interesting incompressible flows of practical interest are driven by a pressure (or a body force) gradient. Typically, these include tube and channel flows with a great variety of geometries. The main difficulty in the numerical simulation of these flows reside in the so-called 'open' boundaries. In closed flows, where the computational domain is completely bounded by solid

* Corresponding author.
E-mail address: ramon.fernandez@uma.es (R. Fernandez-Feria).

doi:10.1016/S0045-7930(03)00062-8

walls, there is no ambiguity in the boundary conditions (BCs) for the incompressible Navier–Stokes (NS) equations: they consist of Dirichlet BCs for the velocity. The pressure, if needed, is usually obtained from a Poisson equation, resulting from the incompressibility constraint, frequently discretized on a staggered grid which does not require pressure BCs (see, for instance, [1, Chapter 17]). However, when open boundaries are present, through which the fluid may enter or leave the domain, there is no general agreement on which kind of BCs are both mathematically correct and physically the most appropriate on these boundaries (see, e.g., [2]). It is not the aim of this paper to add new insight into the general problem of open BCs, but to present a finite-difference scheme for solving the incompressible NS equations in primitive variables (pressure p and velocity $\mathbf{v}$) in which a 'pressure drop' between the 'inlet' and the 'outlet' can be implemented as part of the BCs, and to discuss the limitations on the geometry of the computational domain brought about by this BC.

Flows driven by a pressure drop are usually simulated numerically in primitive variables (we will not discuss here other formulations such as velocity–vector potential, or velocity–vorticity, which, of course, cannot be used to enforce *directly* a pressure difference into the flow) by imposing a given velocity profile at the inlet, and homogeneous Neumann BCs for some velocity components at the outlet. In these computations, the inflow surface(s) is chosen sufficiently far upstream, and the outflow surface(s) sufficiently far downstream, so that the BCs on them do not affect the behaviour of the solution in the region of interest. Once the flow is solved, the given flow rate at the inlet is related to the obtained pressure difference in the region of interest. However, in many applications it would be very convenient to fix the pressure difference at the start, and then obtain the time evolution of the flow, the flow rate, and all the flow properties, associated to that pressure drop. This, of course, would require the specification of the pressure at least on part of the inlet, and on part of the outlet. In addition, as we shall see below, some other velocity requirements have to be enforced on these boundaries for the solution to satisfy the momentum and incompressibility equations on them, which will put some restrictions on the computational choice of these open boundaries.

The finite-difference scheme presented in this paper is based on the projection method, introduced by Chorin [3] and Temam [4], and then extended to high-order time accuracy, with different variations, by many other authors (see, e.g., [5–7] for a recent account). In this method, an intermediate velocity variable $\mathbf{v}^*$, which does not satisfy the incompressibility constraint, is first computed at each time step. Then, the pressure is used to project the tentative velocity into the space of discretely incompressible functions. If the resulting Poisson equation for the pressure is solved with Neumann BCs, which come from the normal component of the momentum equation on the boundaries where Dirichlet BCs for the velocity are specified, the solenoidal constraint for $\mathbf{v}$ applies also at the boundaries (see, e.g., [5,8]). However, if one imposes Dirichlet BCs for the pressure on some boundaries, $\nabla \cdot \mathbf{v} = 0$ is not necessarily satisfied on them (see, e.g., [8,9]). Therefore, one has to apply $\nabla \cdot \mathbf{v} = 0$ as a 'BC' on these surfaces where the pressure is specified. This is somewhat analogous to the extra numerical BC for the pressure proposed by Henshaw [10], but in a very different numerical approach. An additional, and important, problem is that neither the pressure nor the velocity are actually known at the inflow and at the outflow boundaries, so that they have to be obtained as part of the solution. In particular, what we propose in this paper is to specify the pressure only at a closed curve(s) on the inflow surface(s), and at another curve(s) on the outflow surface(s), so that the desired pressure difference is enforced in the flow. Typically, these curves are chosen to be the intersection of the inlet and outlet surfaces with the solid boundaries that confine the flow (these curves are reduced to just a set of points in a two-dimensional flow). Now, a two-dimensional version of the Poisson equation, which enforces the incompressibility constraint, is solved on the inlet and outlet surfaces with the appropriate Dirichlet BCs at the curves where p is given. The resulting pressure is then used as Dirichlet BCs for the three-dimensional pressure Poisson equation. As we shall see, the condition $\partial v_n/\partial n = 0$ on the inflow and outflow surfaces, where n indicates the normal component to the surface, simplifies significantly the implementation of the numerical scheme, but at the cost of putting some additional restrictions on these surfaces.

The prescription of a pressure drop between the inlet at the outlet of the flow was also considered by Heywood et al. [11], but using a variational approach with given *mean* values of the pressure across the inflow and outflow boundaries. This is an approximation which is not needed in the scheme given in the present paper, where both the pressure and the velocity fields on the inflow and outflow boundaries are obtained as part of the solution, satisfying the same NS equations that the interior of the flow, but with the pressure specified at some points on the inlet and outlet surfaces.

In the next section the method is described for a general three-dimensional tube flow. For simplicity sake, it is first introduced using an explicit scheme first-order accurate in time. Then, it is extended to second-order accuracy in time by using a predictor–corrector method. It must be noted here that these general projection schemes are not new; what is new in this paper is the way in which Dirichlet BCs for the pressure are implemented at the inlet and outlet sections for tube flows. The idea of the method can be applied to other finite-difference schemes. To check the accuracy of the method, it is first applied in Section 3 to the pressure driven flow over a backward-facing step. The results are compared with an existing standard numerical solution. In Section 4, the details of the implementation of the method in cylindrical coordinates, using a scheme second-order accurate in space and time, is given together with numerical results for axisymmetric and non-axisymmetric pipe flows. These results are compared with theoretical, and with previous numerical, results. Finally, the conclusions are given in Section 5.

2. Formulation of the method

Consider the tube flows in the general geometries of Fig. 1. Although the numerical method we are going to present here may be used for any incompressible flow where the pressure is specified on part of the boundary, for reasons that will be evident below it is most suited for general tube flows like those depicted in Fig. 1, where S_w and S_{wi} are arbitrary cylindrical surfaces. The selected examples solved in the following sections are a two-dimensional channel flow, and a pipe flow in cylindrical coordinates, but the method can be applied to any curved tube with general cross-section by just writing the incompressible NS equations in the appropriate curvilinear coordinate system (see, for instance, [12]). In Fig. 1, z is the axial coordinate along the tube. The domain V is bounded by the inlet and outlet surfaces S_i and S_o, which are normal to the local axial coordinate z, and by S_w [and S_{wi} in the case of Fig. 1(b)], which are solid walls (the case of several inlet, and/or several outlet, surfaces can also be considered in the formulation given below, but for simplicity sake we shall restrict the presentation to the cases of Fig. 1).

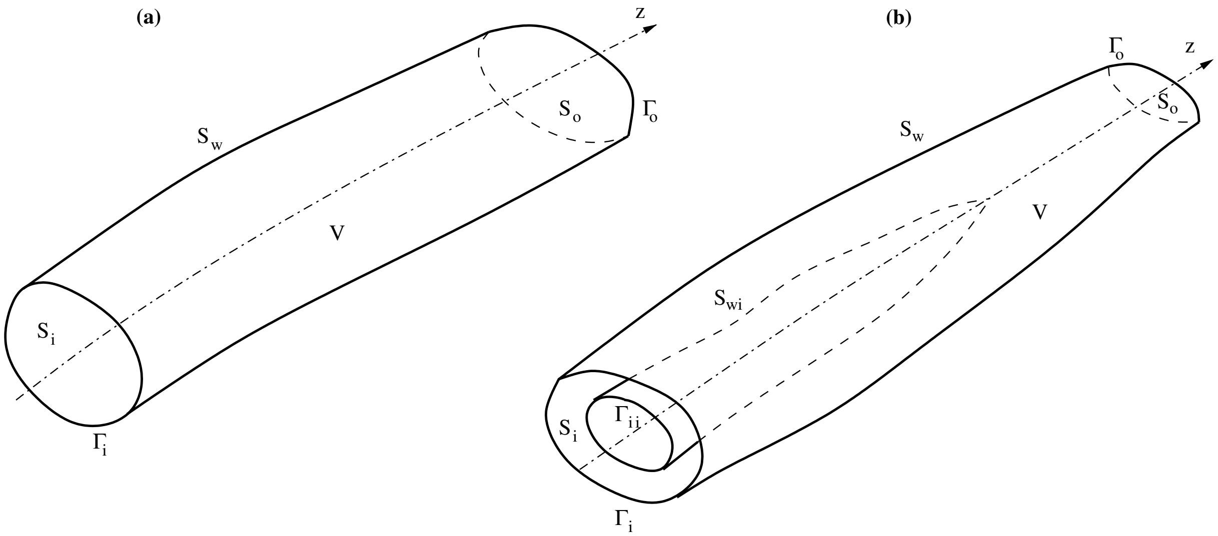

Fig. 1. General tube geometries without (a) and with (b) internal wall.

One is interested in solving the incompressible NS equations in V, which in dimensionless form may be written as

$$\frac{\partial \mathbf{v}}{\partial t} + \mathbf{v} \cdot \nabla \mathbf{v} = -\nabla p + \frac{1}{Re} \nabla^2 \mathbf{v}, \tag{1}$$

$$\nabla \cdot \mathbf{v} = 0. \tag{2}$$

In Eq. (1), the non-dimensional pressure p also includes, as usual, any volume force that can be written in gradient form (such as gravity). Since it is assumed that the flow is driven by a pressure (or/and a body force) difference, we use its characteristic value Δp_c to non-dimensionalize the pressure. Then, the characteristic velocity is $V_c = \sqrt{\Delta p_c/\rho}$, where ρ is the fluid density, and the Reynolds number is defined as

$$Re = \frac{V_c L}{\nu} = \sqrt{\frac{\Delta p_c}{\rho}} \frac{L}{\nu}, \tag{3}$$

with ν, the kinematic viscosity; and L, a characteristic length (a characteristic radius, say).

We want to solve Eqs. (1) and (2) subjected to the BCs that the velocity $\mathbf{v}$ is known on the solid walls, and the pressure p is given on S_i and S_o:

$$\mathbf{v} = \mathbf{v}_w \quad \text{on } S_w \text{ (and } S_{wi}), \tag{4}$$

$$p = p_i \text{ on } S_i, \quad p = p_o \text{ on } S_o, \tag{5}$$

where $\mathbf{v}_w$ is the known velocity of the solid walls which, in general, is a function of time. The inlet and outlet pressure distributions, $p_i(\mathbf{x}, t)$ and $p_o(\mathbf{x}, t)$, are obtained as part of the solution subjected to the conditions

$$p = p_{io}(t) \text{ on } \Gamma_i, \quad p = p_{oo}(t) \text{ on } \Gamma_o, \tag{6}$$

where Γ_i and Γ_o are the contours of S_i and S_o, respectively (see Fig. 1). That is to say, a non-dimensional pressure difference is set between the intersection of S_w with S_i and S_o, which drives the flow inside the tube (in the most common case of a constant pressure drop, one may simply take $p_{io} = 1$ and $p_{oo} = 0$; see the examples in Sections 3 and 4).

2.1. Explicit, first-order accurate in time scheme

Most numerical methods for solving Eqs. (1) and (2) in terms of the primitive variables use a fractional step approach. An approximation to the momentum equation (1) is first made to determine a provisional velocity field, and then an elliptic equation is solved that enforces the solenoidal constraint (2) and determines the pressure. Methods are often called *pressure-Poisson* or *projection* methods depending on which form of the elliptic constraint equation is being used. We shall use a projection method, but with the particularity that Dirichlet BCs are given on part of the boundary, in contrast to the usual Neumann (often homogeneous) BCs used for the pressure on all the boundaries.

To introduce the details of the method, it is convenient to start with an explicit scheme first-order accurate in time. An explicit scheme that is second-order accurate in time will be described in the following subsection. The time-discrete form of Eqs. (1) and (2) are written as

$$\frac{\mathbf{v}^{n+1} - \mathbf{v}^n}{\Delta t} = -\nabla p^{n+1} - \mathbf{v}^n \cdot \nabla \mathbf{v}^n + \frac{1}{Re}\nabla^2 \mathbf{v}^n, \tag{7}$$

$$\nabla \cdot \mathbf{v}^{n+1} = 0, \tag{8}$$

where, as usual, the notation $\mathbf{v}^n$ is used to represent an approximation to $\mathbf{v}(t^n)$, $t^n = n\,\Delta t$. Together with this first-order time discretization one may use a spatial discretization accurate up to any order. In the examples given in Sections 3 and 4 we shall use a finite-difference scheme second-order accurate in space on a non-staggered grid. Staggered grids are used to avoid BCs for the pressure (see, e.g., [13,14]), but in the present method we want to specify the pressure at the inlet and outlet surfaces.

In the projection method, the first step consists on solving an analog to Eq. (7) which yields an intermediate velocity field $\mathbf{v}^*$ that do not satisfy the divergence constraint:

$$\frac{\mathbf{v}^* - \mathbf{v}^n}{\Delta t} = -\mathbf{v}^n \cdot \nabla \mathbf{v}^n + \frac{1}{Re}\nabla^2 \mathbf{v}^n. \tag{9}$$

Since $\mathbf{v}^n$ is known in all the domain V, including the boundaries (at S_w, $\mathbf{v}^n = \mathbf{v}_w$, with $\mathbf{v}_w$ particularized at the instant $n\,\Delta t$), the above explicit method allows to determine $\mathbf{v}^*$ in all the domain V, including the boundaries. That is to say, in the present explicit scheme, no specific BCs are needed for the intermediate velocity field $\mathbf{v}^*$ at each time step [13].

In the second (projection) step one writes, from (7) and (9),

$$\frac{\mathbf{v}^{n+1} - \mathbf{v}^*}{\Delta t} = -\nabla p^{n+1}. \tag{10}$$

An equation for the pressure is then found by taking the divergence of Eq. (10) and using the incompressibility constraint (8)

$$\nabla^2 p^{n+1} = \frac{1}{\Delta t}\nabla \cdot \mathbf{v}^*. \tag{11}$$

The particularity of the present scheme resides in the way in which some of the BCs for this Poisson equation are implemented. On the solid wall S_w (and on S_{wi}), the usual Neumann BCs derived from the normal component of the momentum equation is used [5]. Thus, the normal component to S_w of Eq. (7), taking into account that $\mathbf{v}^{n+1} = \mathbf{v}_w$ on S_w, can be written as

$$\frac{\mathbf{n}\cdot(\mathbf{v}_w - \mathbf{v}^n)}{\Delta t} = -\mathbf{n}\cdot\nabla p^{n+1} + \mathbf{n}\cdot\left[-\mathbf{v}^n\cdot\nabla\mathbf{v}^n + \frac{1}{Re}\nabla^2\mathbf{v}^n\right], \tag{12}$$

where $\mathbf{n}$ is the unit vector normal to S_w. Then, by using Eq. (9), one has the following Neumann BC

$$\mathbf{n}\cdot\nabla p^{n+1} = \frac{1}{\Delta t}\mathbf{n}\cdot(\mathbf{v}^* - \mathbf{v}_w) \quad \text{on } S_w \text{ (and } S_{wi}\text{)}. \tag{13}$$

In this way, the values of the pressure in the grid points on the surface S_w (and S_{wi}) are numerically obtained together with the pressure in the interior points of the domain V by solving the discrete form of the Poisson equation (11), with the consequence that the incompressibility constraint is enforced at all these grid points.

Dirichlet BCs are now specified on the remaining parts of the computational boundary, that is, on S_i and S_o. To obtain the pressure on these surfaces, the two-dimensional 'projection' of the Poisson equation (11) is solved on S_i and S_o (see below for the precise meaning of this 'projection'), with the BCs (6) and the analog to (13) on the contours Γ_i and Γ_o. This procedure is selected to guarantee that, at least, the two-dimensional projection of the incompressibility constraint $\nabla\cdot\mathbf{v}^{n+1} = 0$ is satisfied on S_i and S_o. An additional condition has, therefore, to be applied on S_i and S_o to satisfy the 'whole' divergence constraint on them.

From a practical point of view, this means that the surfaces S_i and S_o cannot be arbitrary, but have to satisfy some requirements. In particular, the implementation is simpler in the case in which S_i and S_o are both normal to the axial coordinate z. In this case, if one writes the velocity on these surfaces as $\mathbf{v} = w\mathbf{e}_z + \mathbf{v}_\tau$, where w is the normal (axial) component of $\mathbf{v}$; and $\mathbf{v}_\tau$, the tangential components, one has to impose the additional BCs

$$\frac{\partial w}{\partial z} = 0 \quad \text{on } S_i \text{ and } S_o. \tag{14}$$

To be more precise, let us consider the inlet surface S_i. The two-dimensional Poisson equation to be solved on S_i is

$$\nabla_\tau\cdot\nabla_\tau p^{n+1} = \frac{1}{\Delta t}\nabla_\tau\cdot\mathbf{v}^*_\tau \quad \text{on } S_i, \tag{15}$$

where ∇_τ is the part of the ∇ operator with derivatives tangent to the surface S_i, and $\mathbf{v}^*_\tau$ is the tangential component of $\mathbf{v}^*$. This equation, together with condition (14), guarantees that $\nabla\cdot\mathbf{v}^{n+1} = 0$ on S_i. The same applies to S_o.

The requirement (14) can be easily met in most tube flow of interest by just selecting computational inlet and outlet surfaces sufficiently far away one of the other (large length to radius ratio). In any case, this is a price that one has to pay for solving numerically the sometimes more realistic and interesting problem with arbitrary Dirichlet BCs for the pressure at the tube ends. Other combinations, different to (14) plus (15), that enforces $\nabla \cdot \mathbf{v} = 0$ on the inflow and outflow boundaries may be envisaged, but the present one seems to be the most appropriate, and the simplest to implement, in tube flows.

Eq. (15) has to be solved with the following BCs on the curve $\Gamma_{\rm i}$

$$p^{n+1} = p_{\rm io} \quad \text{on } \Gamma_{\rm i}, \tag{16}$$

and

$$\mathbf{n} \cdot \nabla p^{n+1} = \frac{1}{\Delta t} \mathbf{n} \cdot (\mathbf{v}^* - \mathbf{v}_{\rm w}) \quad \text{on } \Gamma_{\rm ii}, \tag{17}$$

in the case of an inner wall (Fig. 1b), where $\mathbf{n}$ is now the unit vector normal to $S_{\rm w}$ at $\Gamma_{\rm ii}$. The same procedure applies to $S_{\rm o}$, but with $p^{n+1} = p_{\rm oo}$ on $\Gamma_{\rm o}$ ($p_{\rm io} = 1$ and $p_{\rm oo} = 0$ in the case of a constant pressure drop).

Once p is known on $S_{\rm i}$ and $S_{\rm o}$, one can solve the 3D Poisson equation (11) with Neumann BCs (13) on $S_{\rm w}$ (and $S_{\rm wi}$), and Dirichlet BCs on $S_{\rm i}$ and $S_{\rm o}$. The last step of the method is to update the velocity field at the instant $(n+1)\,\Delta t$ by using Eq. (10):

$$\mathbf{v}^{n+1} = \mathbf{v}^* - (\Delta t)\nabla p^{n+1}. \tag{18}$$

This expression is used to obtain the three velocity components in all the grid points, except for the normal component w in the interior grid points of the surfaces $S_{\rm i}$ and $S_{\rm o}$, which have to be obtained discretizing Eq. (14). Actually, the discrepancy between the values of w obtained in these points from (14), and those obtained by using (18), is a measure of how suitable are the surfaces $S_{\rm i}$ and $S_{\rm o}$ for applying the present Dirichlet BCs for the pressure. In the examples considered in Sections 3 and 4 the differences are very small indeed.

As initial condition, a convenient choice is to start from the fluid at rest, $\mathbf{v}(t = 0) = \mathbf{0}$. No initial condition for the pressure is needed, for the Poisson equation (11) with Dirichlet BCs on $S_{\rm i}$ and $S_{\rm o}$ provides the appropriate initial distribution of p once the first step (9) is solved for the first time. This fact constitutes also a fundamental difference with respect to standard projection methods, where homogeneous Neumann BCs are used for p. The linear system resulting from the discrete Poisson equation is then singular, and has to be solved with a somewhat artificial initial distribution of p. In contrast, with the present method, the flow is driven by a realistic pressure gradient from the start (see examples in the following sections). The only spurious pressure mode is the constant hydrostatic pressure, which is fixed by the value $p_{\rm oo}$ on $\Gamma_{\rm o}$ (say). No other spurious pressure modes, as those discussed, for instance, in [15], appear in this problem because the velocity field is not fixed at the inlet and outlet surfaces, but let to evolve freely according to (1) and (2) and the given pressure difference.

The method can, of course, be applied to the much simpler case of a two-dimensional flow (for instance, the channel flow considered in Section 3 below, or an axisymmetric pipe flow). The computational domain V is then on a plane, and the inlet and outlet surfaces $S_{\rm i}$ and $S_{\rm o}$ are just two segments. Eq. (15) on S_i and S_o are ordinary differential equations on these two lines, which have to be solved with the corresponding BCs on Γ_i and Γ_o, which now become two grid points.

2.2. Explicit, second-order accurate in time scheme

The first-order scheme described above can be easily extended to second-order accuracy in time. In this section we describe the general features of an explicit predictor–corrector method second-order accurate in time, which is the scheme used in the examples solved in the next sections.

It must be noted here that although there is general agreement in that the velocity field can be obtained with second-order (or any order) accuracy in time using a projection method, some authors have argued that the pressure can be determined only to first order in time, and that this is an inherent defect of the projection method (see, e.g., [16–19]). However, Brown et al. [7] have recently shown that this is not always the case, provided that one uses appropriate pressure BCs, and update correctly the pressure. For this reason, to avoid confusion, in this section we shall use a projection function ϕ to designate the result of the projection step, instead of naming it p, and then update the pressure at the end of the time step. We shall see that the method provides second-order accuracy in time, but for a 'lagged' pressure.

In a predictor–corrector scheme, the two steps of the projection method are made twice at each time step. At the predictor stage, one takes a time step $\Delta t/2$, so that, instead of Eqs. (9)–(11), one has

$$\frac{\mathbf{v}^* - \mathbf{v}^n}{\Delta t/2} = -\mathbf{v}^n \cdot \nabla \mathbf{v}^n + \frac{1}{Re}\nabla^2 \mathbf{v}^n, \tag{19}$$

$$\frac{\mathbf{v}^{n+1/2} - \mathbf{v}^*}{\Delta t/2} = -\nabla \phi^{n+1/2}, \tag{20}$$

$$\nabla^2 \phi^{n+1/2} = \frac{2}{\Delta t}\nabla \cdot \mathbf{v}^*. \tag{21}$$

The BCs for $\phi^{n+1/2}$ are formally the same used for p^{n+1} in (13)–(16). Once $\mathbf{v}^{n+1/2}$ is updated from Eq. (20), these values are used in the correction stage to obtain $\mathbf{v}^{n+1}$:

$$\frac{\mathbf{v}^{**} - \mathbf{v}^n}{\Delta t} = -\mathbf{v}^{n+1/2} \cdot \nabla \mathbf{v}^{n+1/2} + \frac{1}{Re}\nabla^2 \mathbf{v}^{n+1/2}, \tag{22}$$

$$\frac{\mathbf{v}^{n+1} - \mathbf{v}^{**}}{\Delta t} = -\nabla \phi^{n+1}, \tag{23}$$

$$\nabla^2 \phi^{n+1} = \frac{1}{\Delta t}\nabla \cdot \mathbf{v}^{**}, \tag{24}$$

where the BCs for ϕ^{n+1} are formally the same used for p^{n+1} in (13)–(16), but now using $\mathbf{v}^{**}$ instead of $\mathbf{v}^*$. Eq. (23) is used to update $\mathbf{v}^{n+1}$ once ϕ^{n+1} is known.

Adding Eqs. (22) and (23), one has

$$\frac{\mathbf{v}^{n+1} - \mathbf{v}^n}{\Delta t} = -\nabla \phi^{n+1} - \mathbf{v}^{n+1/2} \cdot \nabla \mathbf{v}^{n+1/2} + \frac{1}{Re}\nabla^2 \mathbf{v}^{n+1/2}, \tag{25}$$

which is the equation equivalent to the first-order explicit scheme (7) for the present explicit predictor–corrector scheme. According to this expression, not only the obtained velocity field is second-order accurate in time, but also the pressure, if one identifies

$$p^{n+1/2} = \phi^{n+1}. \tag{26}$$

It must be noted that the BCs used for ϕ^{n+1} are the appropriate ones for $p^{n+1/2}$. Thus, one obtains a 'lagged', second-order accurate in time, pressure field [7]. This is corroborated by the numerical examples considered in Section 4.

2.3. Numerical stability of the explicit schemes

Explicit schemes as the ones described in the preceeding sections are known to have severe stability constraints over the time step. An approximate stability analysis of the linearized equations yields the conditions [20]:

$$\tfrac{1}{2}v^2\,\Delta t\,Re \leqslant 1,$$

$$\frac{6\,\Delta t}{\Delta x^2\,Re} \leqslant 1 \quad (\text{if } \Delta x^2 = \Delta y^2 = \Delta z^2).$$

In the examples considered in the following sections, with Reynolds numbers ranging between 100 and several thousands, and for different mesh sizes, the maximum value of Δt ranged between 10^{-3} and 10^{-2}.

This limitation on the time step can be significantly reduced by using implicit, or rather, semi-implicit, methods (see, e.g. [13,21]). As shown by Brown et al. [7], second-order accurate implicit schemes for the pressure are also possible provided that one uses appropriate BCs for the pressure and update it correctly at the end of each time step. The relation between p and ϕ is then much more complex than (26). In addition, with an implicit method one has to impose BCs to solve the equations for the intermediate velocity $\mathbf{v}^*$ [13], which are not needed in the explicit schemes. For these reasons, the numerical implementation of the implicit projection methods are much more complex than the explicit ones, particularly when Dirichlet BCs are used for the pressure, and we do not consider them here. All the following examples are solved using the second-order explicit method of Section 2.2.

3. Flow over a backward-facing step

As a first application of the method, this section considers the two-dimensional channel flow over a backward-facing step. This is a standard problem for which there exists several sources of numerical results to compare with. In particular, we shall compare our numerical results with those of Gartling [22] for a Reynolds number based on the flow rate equal to 800.

The geometry of the flow, non-dimensional co-ordinate system with channel dimensions, and the BCs used are given in Fig. 2. The characteristic length is the channel height H. For $x \geqslant 0$, the channel dimensions $(0 \leqslant x \leqslant 30, -\frac{1}{2} \leqslant y \leqslant \frac{1}{2})$ are the same of [22]. However, because our flow is now driven by a pressure difference between the inlet and the outlet sections, instead of being

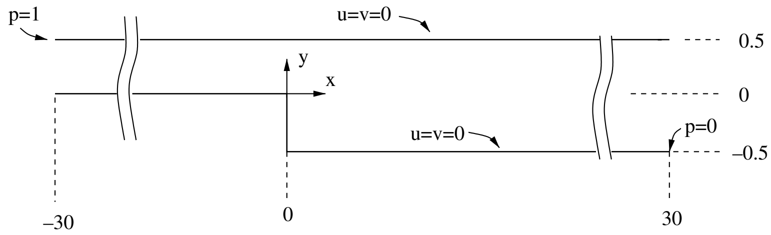

Fig. 2. Backward-facing step geometry with channel dimensions and BCs.

generated by a specified velocity field at $x = 0$, we have to add an inlet region $x < 0$. This is so owing to the fact that the steady state pressure at $x = 0$ for the Reynolds number considered in [22] is smaller than the pressure at the flow exit $x = 30$ (see Fig. 4 below), so that the pressure driven flow cannot be numerically simulated by specifying a pressure difference between $x = 0$ and $x = 30$. In the present numerical simulation we have selected an entrance region ($x < 0$) of the same length $30H$ as the $x \geqslant 0$ region.

For a given Reynolds number, the numerical simulation starts at $t = 0$ with $\mathbf{v} = u\mathbf{e}_x + v\mathbf{e}_y = \mathbf{0}$. The inlet and outlet pressure distributions are obtained from (15) and (16), which in the present problem are rather simple:

$$\frac{\partial^2 p}{\partial y^2} = \frac{1}{\Delta t}\frac{\partial \mathbf{v}^*}{\partial y} \quad \text{on } x = x_{\mathrm{i}} = -30,\ 0 \leqslant y \leqslant 1/2 \text{ and on } x = x_{\mathrm{o}} = 30,\ -1/2 \leqslant y \leqslant 1/2, \tag{27}$$

with the BCs

$$p = 1, \quad \frac{\partial p}{\partial y} = \frac{v^*}{\Delta t} \text{ at } x = x_{\mathrm{i}},\ y = \tfrac{1}{2}, \tag{28}$$

and

$$p = 0, \quad \frac{\partial p}{\partial y} = \frac{v^*}{\Delta t} \text{ at } x = x_{\mathrm{o}},\ y = -\tfrac{1}{2}. \tag{29}$$

With the Dirichlet BCs on the inflow and outflow thus obtained, and with the corresponding Neumann BCs (13) on the solid walls ($y = 1/2$, $x_{\mathrm{i}} \leqslant x \leqslant x_{\mathrm{o}}$; $y = 0$, $x_{\mathrm{i}} \leqslant x \leqslant 0$; $-1/2 \leqslant y \leqslant 0$, $x = 0$; $y = -1/2$, $0 \leqslant x \leqslant x_{\mathrm{o}}$), the pressure Poisson equation (11) yields a realistic pressure distribution from the start, that drives the flow until it reaches a steady state (if it exists). In the numerical simulations reported here we have used the predictor–corrector scheme described in Section 2.2, second-order accurate in space and time, with an uniform mesh of $(n_x = 801) \times (n_y = 41)$ nodes. The time step used was $\Delta t = 5 \times 10^{-3}$, which is close to the maximum value given by the numerical stability of the explicit method.

To check the numerical results, we have simulated the same Reynolds number considered in [22]. This Reynolds number, based on the flow rate Q, is $Re_Q = 800$. Since our Reynolds number (3) is based on the pressure difference, Re_Q is not know a priori: it has to be computed at the end of the numerical simulation from the steady state flow rate obtained with the given Re. The flow rate is in fact a function of time which will be denoted by $q(t)$ [$\lim_{t\to\infty} q(t) \to Q$]. Computing, for instance, the flow rate at the outflow boundary, the relation between q and Δp_{c} can be written as

$$q(t) = \int_{-H/2}^{H/2} \hat{u}\,\mathrm{d}\hat{y} = \sqrt{\frac{\Delta p_c}{\rho}} H \int_{-1/2}^{1/2} u(x = x_o, y, t)\,\mathrm{d}y \equiv \sqrt{\frac{\Delta p_c}{\rho}} H \gamma(t), \tag{30}$$

where $\hat{u}$ and $\hat{y}$ are the dimensional counterparts of u and y, respectively, and γ is the non-dimensional flow rate. Thus, using (3) and the definition

$$Re_q \equiv \frac{2q(t)}{\nu}, \tag{31}$$

one has the following relation between Re and the Reynolds number based on the flow rate:

$$Re_q(t) = 2\gamma(t)Re, \quad \lim_{t\to\infty} Re_q \to Re_Q. \tag{32}$$

For a given Re, at the end of the computations one finds the corresponding Re_Q. For the present geometry (Fig. 2), it is found that $Re_Q = 800$ is reached with $Re \simeq 985$ [see Fig. 3 for the corresponding function $Re_q(t)$]. Fig. 4 shows the time evolution of the horizontal velocity profiles across the channel at four horizontal locations, $x = -15$, 0, 15, and 30.

To compare our results with those given in [22], the following equivalences have to be made:

$$\mathbf{v}_G = \frac{Re}{Re_Q}\mathbf{v}, \quad p_G = \left(\frac{Re}{Re_Q}\right)^2 (p - p_{co}), \quad p_{co} \equiv p(x = 0, y = 0), \tag{33}$$

where the subscript G denotes the non-dimensional variables used by Gartling [22] [note that p_G is zero at the step corner ($x = 0$, $y = 0$)]. Using these variables, Fig. 5(a) shows several pressure distributions along the channel (for $y = 0$, $-1/2$, and 1/2). For $x \geqslant 0$, these distributions practically coincide with those given in Fig. 7 of [22]. Actually, the form of the profiles coincide, but there is a little vertical shift of the profiles. This small shift is better appreciated in Fig. 5(b), where cross-channel profiles of p for $x = 7$ and $x = 15$ are compared with Gartling's results. It is due to the fact that the pressure level is adjusted to be zero at the step corner, where the solution is singular [see Fig. 5(a) at $x = 0$]. Numerical errors are larger at this location due to the sharp gradients of the different variables there, making very sensitive the pressure level to the mesh size (see [22]).

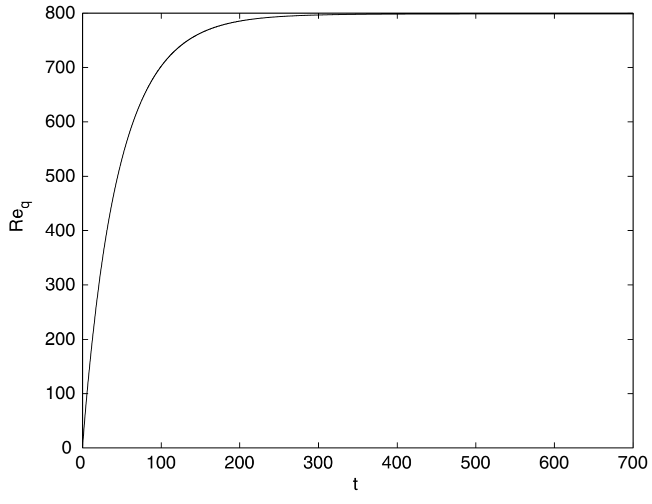

Fig. 3. $Re_q(t)$ for the flow in the channel of Fig. 2 with $Re = 985$ ($Re_Q \simeq 800$).

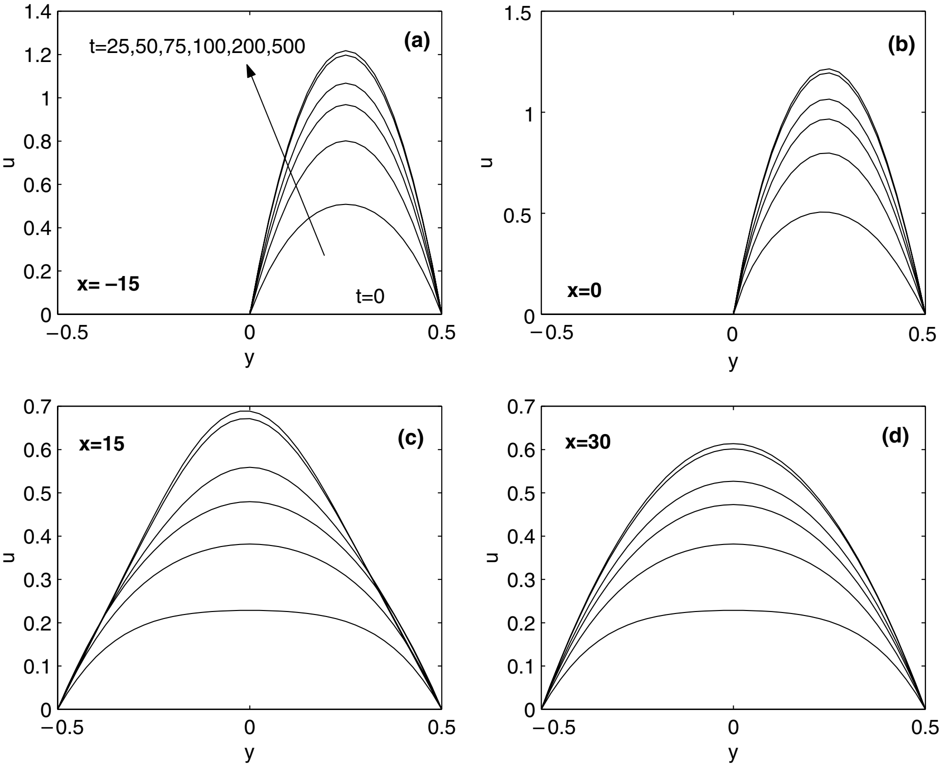

Fig. 4. Time evolution of the horizontal velocity profiles across the channel at $x = -15$ (a), $x = 0$ (b), $x = 15$ (c), and $x = 30$ (d), for the same *Re* of Fig. 3. The instants of time plotted are specified in (a).

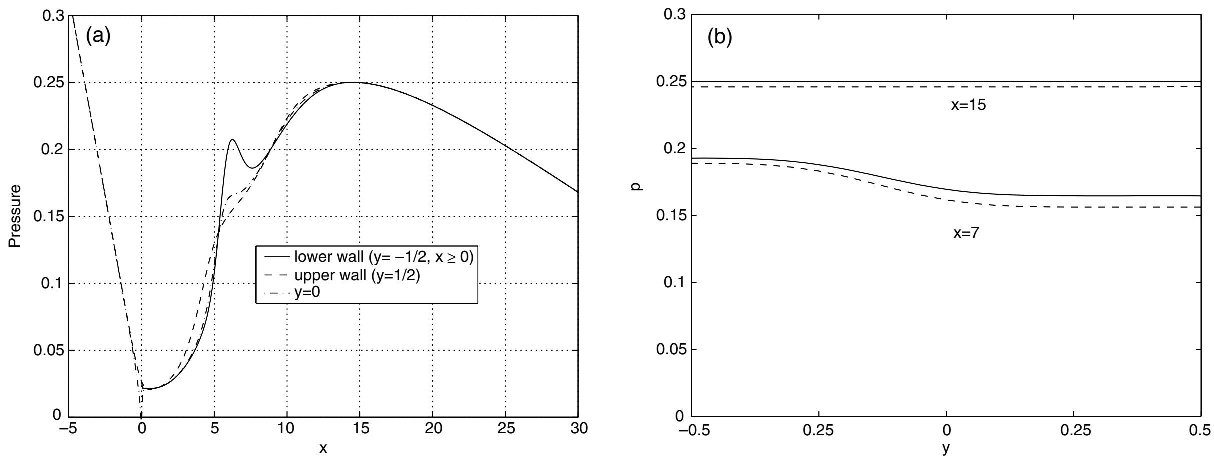

Fig. 5. (a) Steady state pressure profiles along upper and lower channel walls, and along the middle ($y = 0$) of the channel. (b) Pressure profiles across the channel at $x = 7$ and $x = 15$. Dashed lines correspond to the results given by Gartling [22] (from his Tables IV and V).

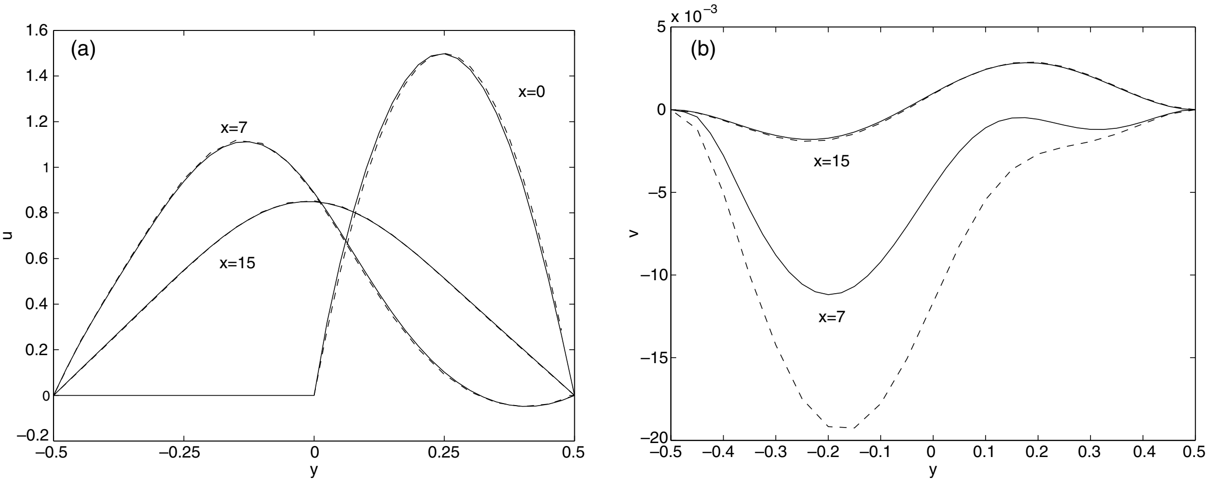

Fig. 6. (a) Steady state horizontal velocity profiles across the channel at $x = 7$ and 15 (dashed lines correspond to the results reported in [22]), and at $x = 0$ (dashed line corresponds to the parabolic velocity profile for $Re_Q = 800$). (b) Vertical velocity profiles across the channel at $x = 7$ and 15 (dashed lines correspond to the results reported in [22]).

Horizontal velocity cross-channel profiles for $x = 7$ and $x = 15$ are plotted in Fig. 6(a). They are almost indistinguishable from the numerical results reported in [22] (dashed lines). Also plotted in that figure is the horizontal velocity at $x = 0$, together with the parabolic Poiseuille profile corresponding to $Re_Q = 800$ (dashed line). It must be noted here that the numerical simulation given in [22] is different to that performed here in that the velocity field is specified at $x = 0$ in [22] (u is given by the parabolic profile plotted in Fig. 6(a), and v is set to zero), while in the present simulation the velocity and pressure profiles evolve from the pressure difference given along the channel. Thus, u is not exactly a parabolic profile at $x = 0$, nor v is zero at $x = 0$, though it is very small. This explains the difference between the vertical velocity profile at $x = 7$ obtained in the present problem and that of [22] [see Fig. 6(b); note that v is very small all over the channel]. However, at $x = 15$ both vertical velocity profiles are almost indistinguishable.

4. Three-dimensional flow in a circular pipe

As a typical 3D pressure driven flow, we consider in this section the flow in a pipe of circular cross-section for several Reynolds numbers. To trigger the three dimensionality in the flow, we consider also the influence of a localized disturbance upstream of the type considered by Ma et al. [23]. Before that, we compare the time evolution of the flow in a circular pipe, with and without rotation of the pipe wall, with available theoretical solutions for the axisymmetric flow.

The numerical results reported below are obtained with the predictor–corrector scheme described in Section 2.2. The equations are written in cylindrical polar coordinates (r, θ, z) [velocity field (u, v, w)], using the radius of the pipe R as the characteristic length $(0 \leqslant r \leqslant 1)$. The numerical scheme is second-order accurate in time, as well as in the spatial directions r and z, and fourth-order accurate in θ. This allows the use of relatively few nodes in the azimuthal direction θ.

To simplify the equations at the axis $r=0$, the dependent variables (ru, rv, rw, p) are used. With these variables, the numerical singularity at $r=0$ of the Poisson equation (21) [and of the Poisson equation (24) in the corrector stage] is more easily avoided using L'Hospital's Rule, to get

$$2\frac{\partial^2\phi}{\partial r^2}+\frac{1}{2}\frac{\partial^4\phi}{\partial r^2\partial\theta^2}+\frac{\partial^2\phi}{\partial z^2}=\frac{1}{\Delta t}\left(\frac{\partial^2(ru)^*}{\partial r^2}+\frac{1}{2}\frac{\partial^3(rv)^*}{\partial r^2\partial\theta}+\frac{\partial^2(rw)^*}{\partial r\partial z}\right)\quad\text{at } r=0, \tag{34}$$

together with the constraints

$$\frac{\partial^2\phi}{\partial\theta^2}=\frac{\partial(rv)^*}{\partial\theta}=0\quad\text{at } r=0,$$

and

$$\frac{\partial\phi}{\partial r}+\frac{\partial^3\phi}{\partial r\partial\theta^2}=\frac{1}{\Delta t}\left(\frac{\partial(ru)^*}{\partial r}+\frac{\partial^2(rv)^*}{\partial r\partial\theta}\right)\quad\text{at } r=0.$$

4.1. Starting Hagen–Poiseuille flow

For the numerical simulations we have used an uniform spatial grid with $(n_r=27)\times(n_\theta=8)\times(n_z=513)$ nodes, in a pipe of length $z_f=32\pi\simeq 100.5$. The pressure is set equal to unity at ($r=1$, $z=0$), and equal to zero at ($r=1$, $z=z_f$) (in both cases for $0\leqslant\theta\leqslant 2\pi$). Except otherwise indicated, the time step was 5×10^{-3}, which is close to the maximum given by the numerical stability for the Reynolds number and the spatial mesh size used. As in the example described in the preceeding section, for a given Re (based on the pressure difference), starting at $t=0$ with the fluid at rest, the flow rate evolves in time until a steady state is reached (if it exists). The instantaneous flow rate (and the corresponding Reynolds number) is computed at the flow exit. The relation between Re and Re_Q is the following:

$$Re_q(t)=Re\frac{1}{\pi}\int_0^{2\pi}\int_0^1 (rw)_{z=z_f}\,\mathrm{d}\theta\,\mathrm{d}r,\quad \lim_{t\to\infty} Re_q\to Re_Q. \tag{35}$$

Fig. 7 shows the time evolution of Re_q for $Re_Q=500$, which for the given pipe length corresponds to $Re=448.4$ [$\simeq(4Re_Qz_f)^{1/2}$]. Both, z_f and Re_Q are selected to compare with [23] (see Section 4.3 below). An almost linear pressure distribution along the pipe is set from the first time step, when the velocity is still zero. Then, the flow evolves from rest, remaining always axisymmetric (in accordance with linear stability theory; see, e.g., [24]), reaching the parabolic streamwise velocity profile corresponding to $Re_Q=500$ all over the pipe, together with $u\simeq v\simeq 0$, as $t\to\infty$. Fig. 8 shows the time evolution of the axial velocity w at $r=1/2$ and $z=z_f/2$ (both for $\theta=0$ and $\theta=\pi$), together with the well-known analytical solution for the transient Hagen–Poiuseuille flow in a pipe, obtained by separation of variables (see, e.g., [25]):

$$W(r,t)=\frac{Re}{4z_f}\left[1-r^2-\sum_{n=1}^{\infty}\frac{8J_0(\lambda_{0n}r)}{\lambda_{0n}^3J_1(\lambda_{0n})}\exp(-\lambda_{0n}^2t/Re)\right], \tag{36}$$

where J_i is the Bessel function of the first kind of order i, and λ_{in} is the nth zero of J_i. It is seen that the agreement is excellent, corroborating that the present method yields physically correct time evolutions of the flow when a pressure difference is set between the inflow and the outflow sec-

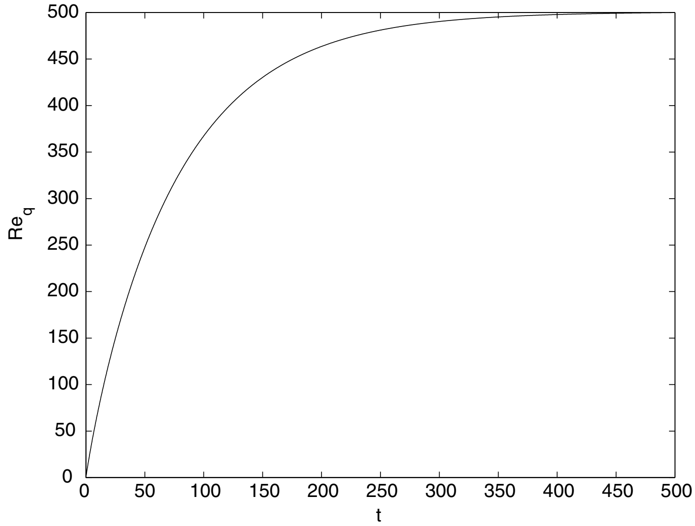

Fig. 7. $Re_q(t)$ for the flow in a pipe of length 32π for $Re_Q = 500$.

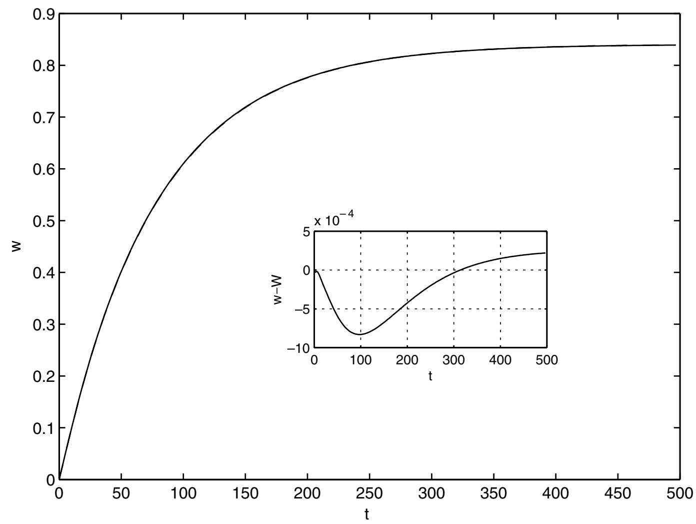

Fig. 8. Temporal evolution of the streamwise velocity w at $r = 1/2$, $z = 32\pi/2$ (half the length of the pipe), and two values of θ ($\theta = 0$ and π; dashed lines), compared to the theoretical axisymmetric value $W(r = 1/2, t)$ given by (36) (continuous line). $Re_Q = 500$. The three curves are almost indistinguishable. The inset shows the difference between the numerical solution w (both at $\theta = 0$ and π) and the theoretical solution W.

tions. Actually, the inset of Fig. 8 shows that the flow remains always axisymmetric (the numerical solutions for $\theta = 0$ and $\theta = \pi$ coincide), and that the difference with the theoretical solution (36) is smaller than $O(\Delta t)$. In fact, the error of the numerical solution, in relation to the theoretical one shown in Fig. 8, is not controlled by the time step, but by the spatial mesh size, for the numerical solutions obtained with smaller values of Δt and the same spatial mesh coincide exactly with that depicted in Fig. 8. For the given Re and mesh size, larger values of Δt cannot be used because the explicit method becomes numerically unstable.

4.2. Starting rotating Hagen–Poiseuille flow

In the above example, the steady state consists on a Hagen–Poiseuille flow, where the pressure varies linearly with z, but it is constant at every section of the pipe. However, the pressure is allow to evolve freely during the numerical computation, including the inlet and the outlet sections. In order to show that the present method yields correctly the radial, as well as the axial, pressure evolution of the flow, including the inflow and outflow boundaries (where the pressure is specified only at their contours), we consider here an example where a known radial pressure distribution is reached at the steady state, namely, the flow in a rotating long pipe. In particular, we consider a pipe of length $z_f = 200$ for $Re_Q = 100$ ($Re \simeq 282.84$), with the pipe wall rotating at a given angular velocity Ω such that the azimuthal Reynolds number, $Re_\theta = \Omega R^2/\nu$, is equal to 30. For these values of Re_Q and Re_θ the rotating pipe flow is linearly stable (see, e.g., [26]), so that the flow will remain, as in the preceeding section, always axisymmetric.

An analytical solution for the transient azimuthal velocity, obtained by separation of variables, is also well known (see, e.g., [27]):

$$V(r,t) = \frac{Re_\theta}{Re}\left[r + 2\sum_{n=1}^{\infty}\frac{J_1(\lambda_{1n}r)}{\lambda_{1n}J_0(\lambda_{1n})}\exp(-\lambda_{1n}^2 t/Re)\right]. \tag{37}$$

Fig. 9 shows the comparison of this solution with the numerical one at ($r = 0.5$, $\theta = 0$, $z = z_f/2$) obtained with a grid of $(n_r = 25) \times (n_\theta = 8) \times (n_z = 1001)$ nodes, and $\Delta t = 5 \times 10^{-3}$. The agree-

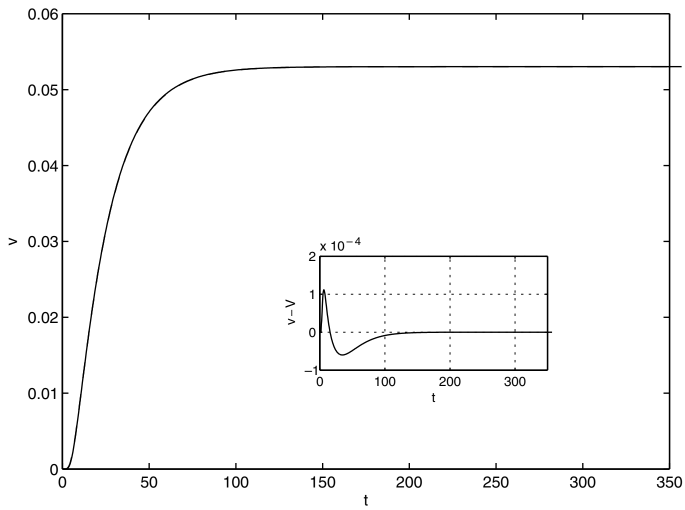

Fig. 9. Temporal evolution of the azimuthal velocity v at $r = 1/2$, $z = 100$ (half the length of the pipe), and $\theta = 0$ (dashed line), compared to the theoretical axisymmetric value $V(r = 1/2, t)$ given by (37) (continuous line). $Re_Q = 100$, $Re_\theta = 30$. The two curves are almost indistinguishable. The inset shows the difference between the numerical solution v and the theoretical solution V.

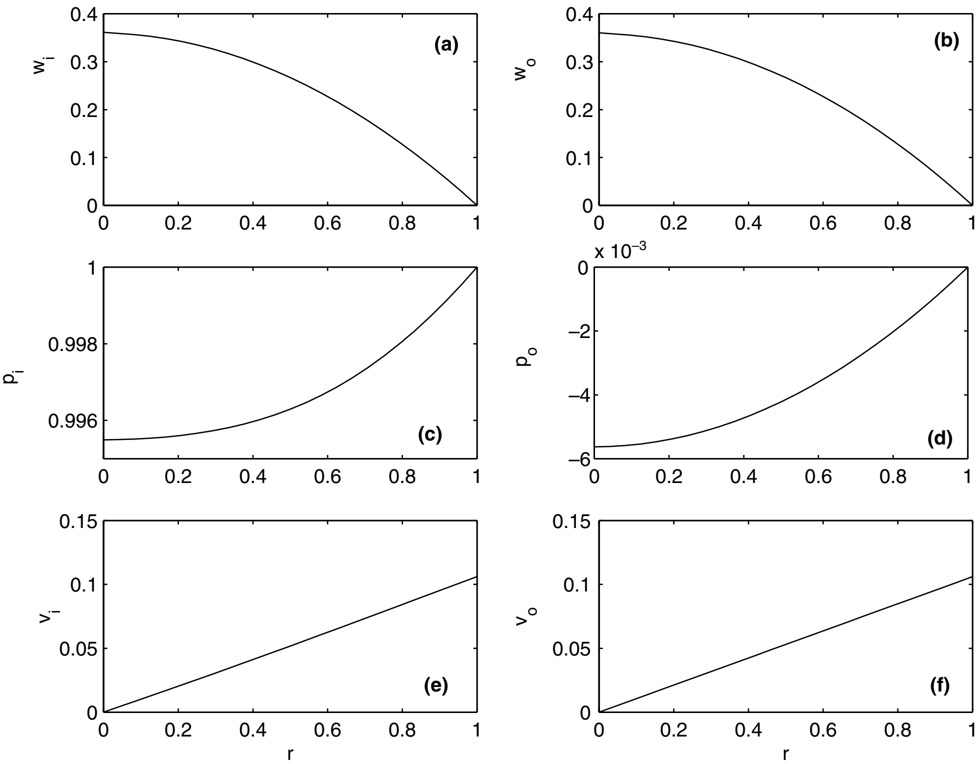

Fig. 10. Steady state ($t \simeq 350$) axial velocity (a,b), pressure (c,d), and azimuthal velocity (e,f) profiles at the inlet ($z = 0$, subscript i) and outlet ($z = z_f$, subscript o) sections (all the curves are for $\theta = 0$). $Re_Q = 100$, $Re_\theta = 30$, $z_f = 200$. They coincide with a solid-body rotation superimposed to a Hagen–Poiseuille flow.

ment is excellent, corroborating again the second-order accuracy in time of the numerical scheme used (as in the preceeding example, the numerical errors in Fig. 9 are not controlled by Δt, but by the spatial mesh size). Fig. 10 depicts the steady state ($t = 350$) radial profiles at the inlet and outlet sections of the axial and azimuthal velocity components, and the pressure. As expected, the axial velocity profile is the parabolic Poiseuille flow, the azimuthal velocity profile is linear, corresponding to a solid-body rotation, and the pressure profile is parabolic, in accordance with the steady state radial momentum equation. Thus, this example corroborates again that the velocity and the pressure should not be specified neither at the inlet nor at the outlet, but they are part of the computation provided that the pressure is given on Γ_i and Γ_o.

4.3. Non-axisymmetric, 3D flow

To trigger three dimensionality in the flow inside the pipe, once Hagen–Poiseuille flow is reached for a given Re, we have also simulated the flow with disturbances at the pipe wall. In particular, in order to compare with previous numerical simulations, we have implemented the same periodic suction and blowing (PSB) disturbances used by Ma et al. [23]. This disturbance of the radial velocity, imposed through a slot located at some position along the pipe wall, is given by

$$u_{\rm dis} = A\tfrac{1}{2}[\cos(2z) + 1]\sin(\theta)\sin(\omega t), \quad r = 1, \;\; 0 \leqslant \theta \leqslant 2\pi, \;\; \pi \leqslant z \leqslant 2\pi, \tag{38}$$

where A is the disturbance amplitude and ω, the disturbance frequency.

It must be noted that the numerical method used by Ma et al. [23] is quite different to the present one. In addition, their simulation differ with the present one in that these authors specify a Hagen–Poiseuille velocity field at the inflow boundary, and, what is more relevant, in that a fringe region of a certain length is added to the end of the pipe with the objective of damping out the disturbance back to Hagen–Poiseuille flow. Neither of these two features are necessary with the present numerical method, where the inflow and the outflow velocity fields are left to evolve freely. Fig. 11 shows temporal evolutions of the pressure at the pipe exit for $r = 1/2$ and two values of θ ($\theta = 0$ and $\theta = \pi$), for $Re_Q = 500$ and 3000, when a disturbance with $\omega = 0.5$ and $A = 0.031$ is imposed on the corresponding Hagen–Poiseuille flow. For a particular instant of time after the disturbance has been introduced into the flow ($t = 26 \times 2\pi/\omega$), Figs. 12(a) and 13(a) show, in a z, θ cross-section of the pipe at $r = 0.5$, the difference between the streamwise velocity w and the axial velocity W of the initial Hagen–Poiseuille flow, for $Re = 500$ and 3000, respectively. For the same values of Re and the same instant of time, Figs. 12(b) and 13(b) show several 3D isosurfaces of the streamwise streaks $w - W$. For $Re_Q = 500$ [Fig. 11(a) and 12], it is observed that the disturbance is damped out along the pipe, and the flow becomes axisymmetric, with Hagen–Poiseuille velocity profile, before exiting the pipe. However, for $Re_Q = 3000$, the disturbances first grow in time during a transient period [see Fig. 11(b)], and then their amplitude decrease. But they are not damped out. In fact, since what is fixed along the pipe is not the flow rate, but the

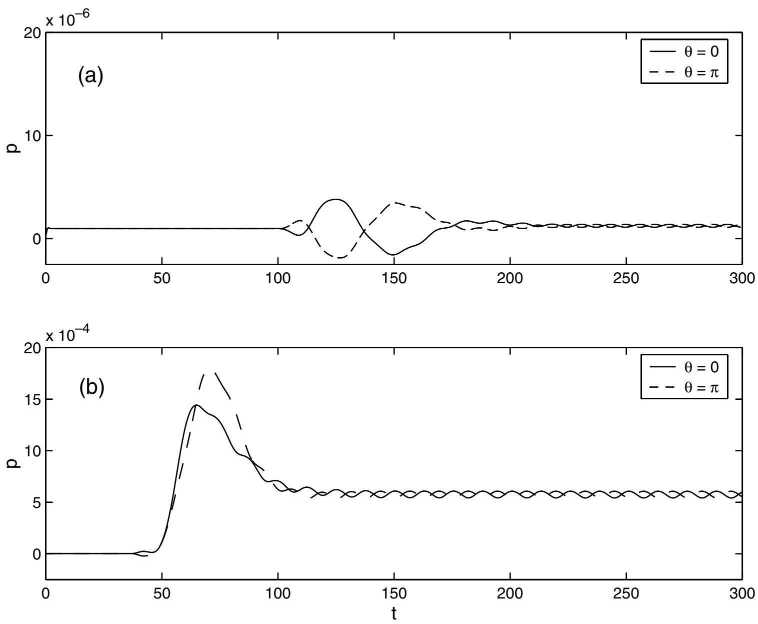

Fig. 11. Time evolution of the pressure, after a disturbance with $A = 0.031$ and $\omega = 0.5$ is set in the flow, at the pipe exit ($z = 32\pi$), $r = 1/2$, and two values of θ (as indicated), for $Re_Q = 500$ (a), and for $Re_Q = 3000$ (b). Note that the pressure scale in (b) is two order of magnitude larger than in (a).

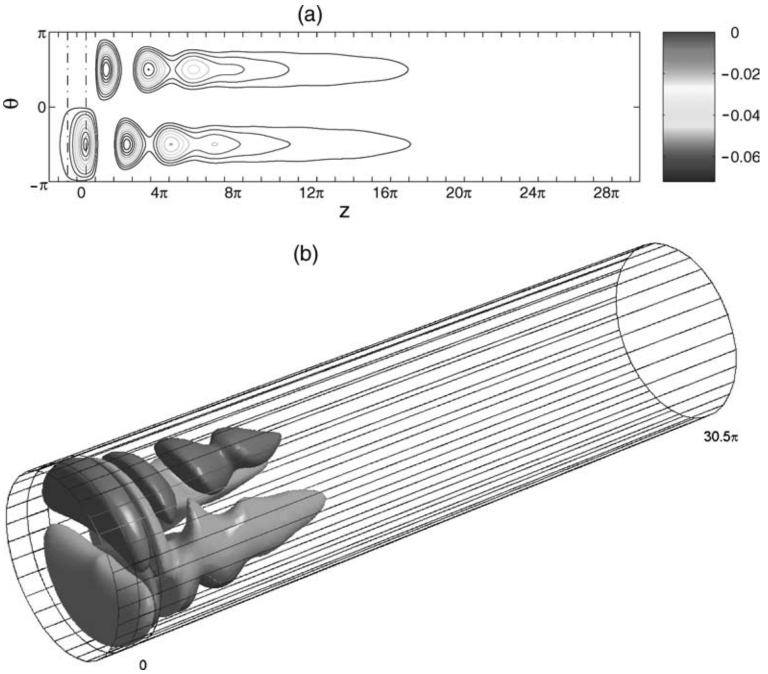

Fig. 12. (a) Instantaneous streamwise streaks $w - W$ at $t = 26 \times 2\pi/\omega$, shown in a z, θ cross-section at $r = 0.5$, for $Re_Q = 500$; disturbance's amplitude $A = 0.031$, and frequency $\omega = 0.5$. The '$- \cdot -$' line delimit the region where the disturbance is introduced into the flow. (b) 3D view of the streamwise streaks $w - W$, represented by the isosurfaces -0.01 (darker one) and 0.01.

Reynolds number based on the pressure difference, the value of Re_Q after the transient is not longer 3000, but slightly smaller (for the time plotted in Fig. 13, $Re_Q \simeq 2976$). The results plotted in Fig. 13 may be compared with those obtained by Ma et al. [23] for the same value $Re_Q = 3000$, and for the same disturbance characteristics (A and ω) and pipe length. The streamwise streaks shown in Fig. 13 are quite similar to those depicted in Figs. 19 and 20 of [23], in spite of the essential differences in the numerical method and in the outflow and inflow BCs. This shows that the present numerical method simulates correctly the three-dimensional features of the flow in the circular pipe.

5. Conclusions

This paper presents a finite-difference projection method for solving, in primitive variables, the incompressible NS equations in open flows where Dirichlet BCs for the pressure are given on part of the boundary. The way in which the pressure BCs are imposed is specially suited for solving tube and channel flows driven by a pressure (or body force) difference. At each time step, the pressure on the inflow and outflow boundaries are obtained from their given value at the contour of these surfaces using a two-dimensional form of the pressure Poisson equation, which enforces the incompressibility constraint. The obtained pressure in these surfaces is then used as Dirichlet BCs for the pressure Poisson equation inside the domain. The implementation of the method is

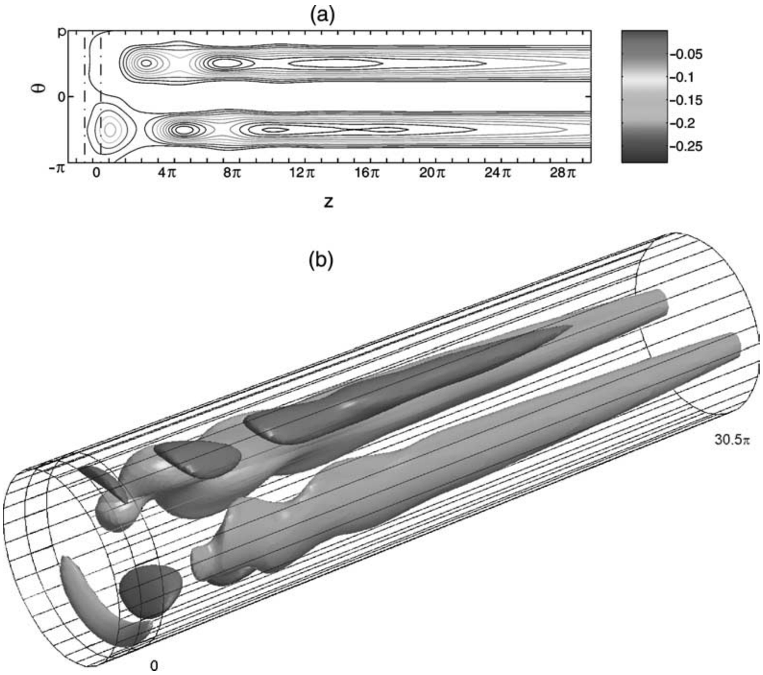

Fig. 13. As in Fig. 12, but for $Re_Q = 3000$. The isosurfaces plotted in (b) are −0.25 (darker one) and 0.15.

presented for several (known) explicit numerical schemes. In particular, an explicit scheme with second-order accuracy in space and time is used to evaluate the qualities of the method by comparing the results for two-dimensional, axisymmetric, and three-dimensional flows with those obtained by other numerical methods, and theory. The comparison was satisfactory in all cases. One of the main advantages of the method is that no velocity field has to be specified on the inflow and outflow boundaries: the velocity (and the pressure) adjust itself in a natural way to the imposed pressure difference. We think that this method is of interest for the simulation of three-dimensional pipe flows, especially for stability and transition studies.

Acknowledgements

This research has been supported by the Ministerio de Ciencia y Tecnología of Spain (grant no. BFM00-1323). Comments and suggestions by Dr. Joaquin Ortega-Casanova are gratefully acknowledged.

References

[1] Fletcher CAJ. Computational techniques for fluid dynamics. Springer-Verlag; 1991.
[2] Sani RL, Gresho PM. Resume and remarks on the open boundary condition minisymposium. Int J Numer Meth Fluids 1994;18:983–1008.

[3] Chorin AJ. Numerical solution of the Navier–Stokes equations. Math Comput 1968;22:745–62.
[4] Temam R. Sur l'approximation de la solution des equations de Navier–Stokes par la methode des pas fractionnaries II. Archiv Ration Mech Anal 1969;33:377–85.
[5] Orszag SA, Israeli M, Deville MO. Boundary conditions for incompressible flows. J Sci Comput 1986;1:75–111.
[6] Karniadakis GEM, Israeli M, Orszag SA. High-order splitting methods for the incompressible Navier–Stokes equations. J Comput Sci 1991;97:414–43.
[7] Brown DL, Cortez R, Minion ML. Accurate projection methods for the incompressible Navier–Stokes equations. J Comput Phys 2001;168:464–99.
[8] Gresho PM, Sani RL. On pressure boundary conditions for the incompressible Navier–Stokes equations. Int J Numer Meth Fluids 1987;7:1111–45.
[9] Gresho PM. Incompressible fluid dynamics: some fundamental formulation issues. Ann Rev Fluid Mech 1991;23:413–53.
[10] Henshaw WD. A fourth-order accurate method for the incompressible Navier–Stokes equations on overlaping grids. J Comput Phys 1994;113:13–25.
[11] Heywood JG, Rannacher R, Turek S. Artificial boundaries and flux and pressure conditions for the incompressible Navier–Stokes equations. Int J Numer Meth Fluids 1996;22:325–52.
[12] Xue L. Study on laminar flow in helical circular pipes with Galerkin method. Comput Fluids 2002;31:113–29.
[13] Kim J, Moin P. Application of a fractional-step method to incompressible Navier–Stokes equations. J Comput Phys 1985;59:308–23.
[14] Verzicco R, Orlandi P. A finite-difference scheme for three-dimensional incompressible flows in cylindrical coordinates. J Comput Phys 1996;123:402–14.
[15] Leriche E, Labrosse G. High-order direct Stokes solvers with or without temporal splitting: Numerical investigations of their comparative properties. SIAM J Sci Comput 2000;22:1386–410.
[16] Temam R. Remark on the pressure boundary condition for the projection method. Theoret Comput Fluid Dynam 1991;3:181–4.
[17] Perot JB. An analysis of the fractional step method. J Comput Phys 1993;108:51–8.
[18] Weinan E, Liu JG. Projection method I: convergence and numerical boundary layers. SIAM J Numer Anal 1995;32:1017–57.
[19] Strikwerda JC, Lee YS. The accuracy of the fractional step method. SIAM J Numer Anal 1999;37:37–47.
[20] Peyret R, Taylor TA. Computational methods for fluid flow. Springer-Verlag; 1983.
[21] Petersson NA. Stability of pressure boundary conditions for Stokes and Navier–Stokes equations. J Comput Phys 2001;172:40–70.
[22] Gartling DK. A test problem for outflow boundary conditions—flow over a backward-facing step. Int J Numer Meth Fluids 1990;11:953–67.
[23] Ma B, van Doorne CWH, Zhang Z, Nieuwstadt FTM. On the spatial evolution of a wall-imposed periodic disturbance in pipe Poiseuille flow at $Re = 3000$. Part 1. Subcritical disturbance. J Fluid Mech 1999;398:181–224.
[24] Salwen H, Grosch CE. The stability of Poiseuille flow in a pipe of circular cross-section. J Fluid Mech 1972;54:93–112.
[25] Batchelor GK. An introduction to fluid dynamics. Cambridge University Press; 1967.
[26] Fernandez-Feria R, del Pino C. The onset of absolute instability of rotating Hagen–Poiseuille flow: a spatial stability analysis. Phys Fluids 2002;14:3087–97.
[27] Pozrikidis C. Fluid dynamics. Theory, computation, and numerical simulation. Kluwer; 2001.